

Intensification of Alkaline Electrolyzer with Improved Two-Phase Flow

Franz Egert, Dirk Ullmer, Sven Marx, Ehsan Taghizadeh, Tobias Morawietz, Martina Gerle, Thi Anh Le, Lucia Paula Campo Schneider, Indro Shubir Biswas, Richard E. Wirz, Philipp Spieth, Tonja Marquard-Möllenstedt, Andreas Brinner, Ricardo Faccio, Luciana Fernández-Werner, Martín Esteves, Fatemeh Razmjooei,* and Syed Asif Ansar

Green hydrogen produced through water electrolysis offers a promising pathway to global decarbonization. Among various electrolyzers, alkaline water electrolysis (AWE) is the most established and commercially mature. To reduce the cost of hydrogen production from AWE, it is crucial to increase operational current density while maintaining or lowering voltage to increase hydrogen yield and reduce energy consumption. Such efforts are focused on reducing the ohmic resistance at high current densities through the implementation of alkaline membranes. However, this work underlines that the ohmic resistance at high current densities is also influenced by the losses associated with the evolution of bubbles at the electrode surface and two-phase mass transfer. This is shown by investigating the impact of tortuosity and bubble point of porous electrodes on AWE performance. Low-tortuosity porous nickel electrodes are fabricated and analyzed for their ability to reduce capillary pressure and bubble point, resulting in lower energy losses and improved efficiency. The cell reaches an industrially appealing relevant current density of 2 A cm⁻² at ≈2 V. Besides test in single cells, the advantageous effect of these low tortuosity porous nickel electrodes are also validated in a kW-class AWE stack, confirming their effectiveness in enhancing overall system performance.

1. Introduction

Global carbon dioxide (CO₂) emission, the most important greenhouse gas (GHG), rebounded in 2021 to 36.3 Gt, driven by a sharp rise in the use of coal in the power sector.^[1] The rate of increase in the GHG emission jeopardizes Paris Agreement temperature targets.[2] The Mission 2020 was launched to accelerate actions and approaches toward the 2030 emission reduction targets that align with the goals of the Paris Agreement reaching net zero emission by the middle of the century.[3,4] Hydrogen (H2) has been recognized as a decisively valuable versatile energy carrier and a key component for the zero-carbon energy system for addressing climate change.[5-11] From a technological point of view, there are four main H₂ production methods: i) hydrocarbon reforming, ii) hydrocarbon pyrolysis, iii) biomass processing, and iv) water splitting.^[12] Among these, green

F. Egert, D. Ullmer, S. Marx, T. Morawietz, M. Gerle, T. A. Le, L. P. Campo Schneider, I. S. Biswas, F. Razmjooei, S. A. Ansar

Institute of Engineering Thermodynamics

German Aerospace Center

Pfaffenwaldring 38-40, 70569 Stuttgart, Germany

E-mail: Fatemeh.Razmjooei@dlr.de

F. Egert

Faculty 6-Aerospace Engineering and Geodesy University of Stuttgart

70569 Stuttgart, Germany

The ORCID identification number(s) for the author(s) of this article can be found under https://doi.org/10.1002/aenm.202405285

© 2025 The Author(s). Advanced Energy Materials published by Wiley-VCH GmbH. This is an open access article under the terms of the Creative Commons Attribution License, which permits use, distribution and reproduction in any medium, provided the original work is properly

DOI: 10.1002/aenm.202405285

E. Taghizadeh, R. E. Wirz Department of Mechanical and Aerospace Engineering University of California Los Angeles, 420 Westwood Plaza, Los Angeles, CA 90095, USA

T. Morawietz Faculty of Science

Energy and Building Services

Esslingen University of Applied Sciences

Kanalstraße 33, 73728 Esslingen am Neckar, Germany

P. Spieth, T. Marquard-Möllenstedt, A. Brinner

Zentrum für Sonnenenergie- und Wasserstoff-Forschung

Baden-Württemberg (ZSW)

Meitnerstraße 1, 70563 Stuttgart, Germany

R. Faccio, L. Fernández-Werner, M. Esteves

Área Física

DETEMA Facultad de Química

Universidad de la República

Av. Gral. Flores 2124, CC 1157, Montevideo CP 11800, Uruguay



www.advenergymat.de

 H_2 , produced by splitting water via electrolysis utilizing renewable power feedstock, is the most suitable one for the transition toward sustainable and secure energy pathways. [13–18] The EU hydrogen strategy, adopted in July 2020, states that green H_2 is crucial for deep decarbonization and aims to accelerate the development of clean H_2 . [19] The goal is to reach the strategic objective of 2×40 GW electrolyzer capacity by 2030, [20] along with increasing the cumulative investments in renewable H_2 in Europe to 180–470 billion \pounds by 2050. [21] This large-scale deployment of electrolyzers for the production of green H_2 , can accelerate the decarbonization process at a significant scale and support the EU's efforts to transition to a climate-neutral society in 2050 while also helping global efforts to implement the Paris Agreement.

For water electrolysis, several technologies are available including well-matured alkaline water electrolysis (AWE), proton exchange membrane water electrolysis (PEMWE), solid oxide electrolysis (SOEL), and others. [17,22-24] Investment costs represent a key challenge and may determine which technology is the most adopted system design for a large-scale application. [17] The investment costs for AWE are reported to be much lower than PEMWE per kW. [17] The high cost is thus a prominent barrier impeding large-scale application of PEMWE. [25] Moreover, the lifetime of AWEs is higher and the annual maintenance costs are lower than those of PEMWE systems. [17] In addition, performing electrolysis under alkaline conditions and a less corrosive environment allows the use of non-noble metal-based catalysts and non-critical material components. [26]

Despite of all these superiorities, AWE has the disadvantage that it typically operates at lower energy efficiency and lower production rate, (with current densities limited to 0.2-0.4 A cm⁻²),^[27-30] when compared to that of PEMWE with more flexible operation at high current density and efficiency. The low current density negatively impacts system size and H2 production costs.[22,31] Consequently, it is feasible that operation at much higher current densities could not only reduce the effective costs of the stack by reducing the stack size but also increase the amount of H₂ production. Therefore, increasing the operational current density and voltage efficiency of AWEs will enable more competitive industrial production of H₂ gas with these systems. [26,32] AWEs are traditionally operated at low current densities due to high internal ohmic resistance.[30,33] In order to operate the AWE at high current densities, one effective strategy can be minimizing the ohmic resistance. However, it is worth mentioning that the ohmic resistance in zero-gap configurations was consistently found to be much higher than that of the separator, due to the gaseous evolution in a zero-gap configuration between the separator and electrodes.^[24] Formation of gases between separator and electrodes in zero-gap configurations are inevitable; because of this, it is not straightforward to completely eliminate the bubbles, which become trapped between the separator and electrodes although they can be reduced. Ohmic resistance, which is mainly influenced by the ohmic resistance of the separator, can also be affected by the structure of the electrodes and the gas bubbles formed.[8] The first approach of replacing a conventional Zirfon separator with an alkaline membrane currently suffers quite significantly from the low durability of the membrane.[34]

This work investigates an alternative approach, which can also cause reducing the ohmic resistance. This consists of investi-

gating the effect of electrode porosity and structures on improving mass transport and in particular favoring bubble formation and transport away from electrode surface and separators. Active electrodes with a suitable combination of micro and large pore size distributions could drastically decrease the ohmic resistance due to their extrinsic activity toward bubble removal. Consequently, the active surface of electrodes remains available for reactions to continue enabling the operation of AWEs at higher current densities while maintaining high efficiency.[18] Enormous efforts have been dedicated so far toward ameliorating the intrinsic and surface activity of electrocatalysts.[26,35-40] Such efforts are still lacking application in full cells or stack operating at high current densities. This is primarily because increasing the operational current density leads to higher gas bubble formation, [26] which in turn blocks a large portion of the active surface area of electrodes and causes significant ohmic resistance, hindering the voltage efficiency specifically at large current densities.[18] The benefits of highly active electrocatalysts thus become minimized. This work therefore suggests that it is very important to increase the electrodes' extrinsic activity, to enable operations of AWE at high current densities. An explanation of the mass-transport behavior of the electrode might then be realized through further understanding of the morphology of its porous structure. For fuel-gas-diffusion layers, the pore-size distribution is as important as total porosity for obtaining high performance. The most effective structure appears to be a combination of small pores with a high contact area and bigger pores with a low tortuosity for effective high-mass transport.[8,41]

Herein, we evaluate porous non-noble metal-based electrodes, namely Ni-based electrodes, for cathodic and anodic reactions of AWE electrolyzer on top of a Ni substrate fabricated using a thermal spraying technique. The AWE electrolyzer cell with fabricated electrodes was evaluated in combination with Zirfon Perl UTP 500. Via extensive physical, electrochemical, and numerical modeling characterizations, we deliver deep insights into the mass transport phenomena of the electrodes and discuss the role of porosity and pore size distribution of electrodes on tortuosity and bubble point of electrodes as well as their respective effects on ohmic resistance and overall cell performance aiming high current density operation. It is found that an electrode with high porosity and large pore size distributions lowers the tortuosity and bubble point, which consequently increases the AWE current densities. This could be due to high porosity and the appropriate pore size distribution, which results in much better bubble removal at higher current densities and therefore lower ohmic resistance. The AWE electrolyzer cell with porous Ni-based electrodes shows a significant reduction in ohmic resistance compared to the bare Ni substrate (with low porosity and inappropriate pore size distributions), which consequently results in a cell with high performance. The AWE electrolyzer cell based on the fabricated nickel-based-electrodes in combination with Zirfon shows 2 A cm⁻² at \approx 2 V. Finally, the functionality of the non-noble electrodes in terms of current density, efficiency, and durability was successfully validated in a 2 kW AWE stack, which shows a high performance of 1.76 V at 0.8 A cm⁻² with the efficiency of 69.7%LHV with no performance degradation at constant current densities of 0.4 and 0.6 A cm⁻² in total for 1534 h.

16146840, 0, Downloaded from https://onlinelibrary.wiley.com/doi/10.1002/æmm.202405285 by Disch Zentrum F. Luft-U. Raum Fahrt In D. Helmholtz Gemein., Wiley Online Library on [13/02/2025]. See the Terms and Conditions (https://onlinelibrary.wiley

and-conditions) on Wiley Online Library for rules of use; OA articles are governed by the applicable Creative Commons

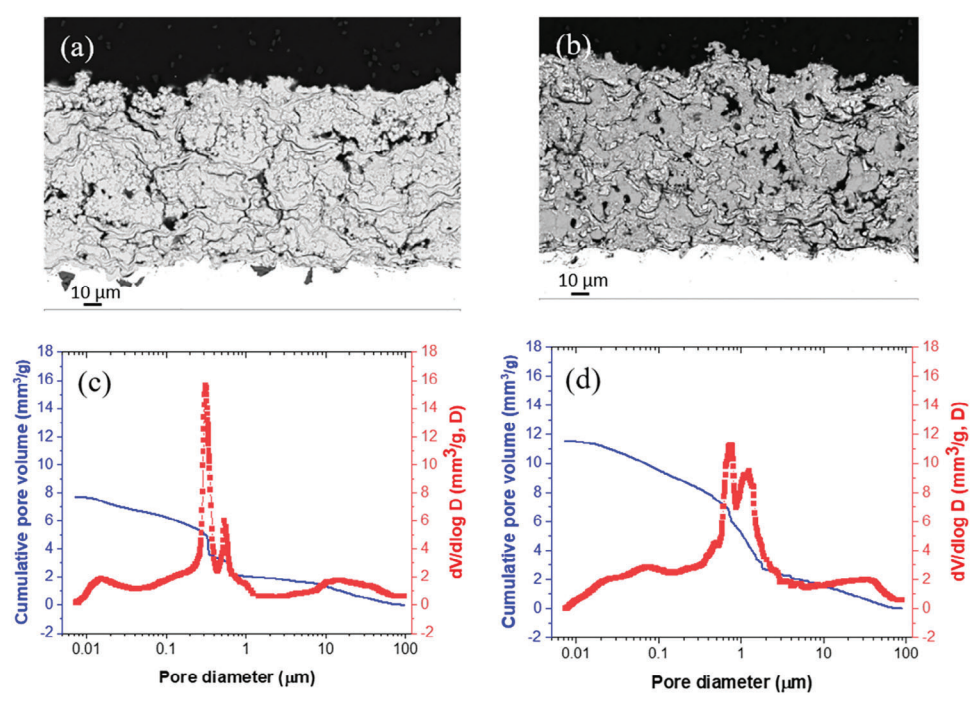


Figure 1. Cross-section SEM images of a) coated porous Ni-based anodic electrode b) coated Mo incorporated porous Ni cathodic electrode. Pore-size distributions and cumulative pore volume calculated by MIP forc) coated porous Ni-based anodic electrode d) coated Mo incorporated porous Ni cathodic electrode.

2. Results and Discussion

A porous Ni-based electrode as an anode and Molybdenum (Mo) incorporated porous Ni as a cathode electrode on the top of nickel mesh (NM) substrate are fabricated using a thermal spray technique. The initial powder precursors for electrode fabrication consist of Al as a pore-forming agent, which is partially removed by further chemical activation of as-prepared electrodes. Array diffraction (XRD) analysis is used for phase identification of both coated anodic and cathodic electrodes, Figure S1a,b (supporting information), respectively. The phase constituent of the anodic porous Ni-based electrode mainly consists of Ni₂Al₃ and NiAl and for Mo incorporated porous Ni electrode mainly consists of Ni₂Al₃, NiAl, Al₃Ni, Mo_{1.08}Ni_{2.93} and MoNi.

To investigate the topological features and properties of the prepared spongy-based electrodes, the microstructure of the electrode surface was analyzed by scanning electron microscopy (SEM). SEM micrographs of anodic porous Ni-based electrodes and cathodic Mo incorporated porous Ni electrodes are shown in Figure 1a,b. The SEM images for both samples show a porous sponge-like structure with several gaps between layers and some open pores for electrodes. Such porosity can potentially facilitate the mass transport of electrolyte and gaseous products which increase bubble emission from the electrode surface specifically at higher current densities. The higher magnification SEM images for both coated anode and cathode are shown in Figure S2a,b (Supporting Information), showing the spongy-like structures for both materials but with wider range of pores for coated cathode. The presence of Ni, Al, Mo, and O is determined by energy dispersive X-ray (EDX) spectroscopy measurements. As

shown in Figure S3 (Supporting Information), elemental mapping images for coated anode Ni-based electrode and coated cathode Mo incorporated porous Ni electrodes indicate the existence of Ni, Al, and O and Ni, Mo, Al and O, respectively. The presence of oxygen suggests partial Ni oxidation at high temperatures during the thermal spraying and partial surface passivation during the chemical activation of the electrode prior to use in an alkaline solution (for more details see Experimental section). [8,42]

Mercury intrusion porosimetry (MIP) is employed to evaluate the total porosity, pore size distribution, and pore volume of the coated electrocatalyst layer on the NM substrates. The results are collected and displayed in double y-axis plots of cumulative pore volume and logarithmic differential pore volume distribution (dV/dlogD) versus pore diameter. First, the calculated total porosity obtained from MIP analysis uncovered the porosity of 25% for coated anode Ni-based electrode and 41% for coated cathode Mo incorporated porous Ni; both are significantly larger than that of bare NM substrate (obtained by MIP), Figure S4 (Supporting Information). Note that the total porosity does not reveal precise information regarding constituent pore size distribution and, accordingly, pore volume. It can be seen clearly in SEM images, Figure 1a,b, that the micropores with wide range exist in activated electrodes. Figure 1c,d exhibit the cumulative porevolume and pore-size distribution curves for coated anode Nibased electrode and coated cathode Mo incorporated porous Ni, respectively. The left y-axis is the cumulative pore-volume curve, which is plotted as a function of the pore diameter. The total pore volumes are 7.7 and 11.5 mm³g⁻¹ for coated anode and coated cathode, respectively. The right y-axis is the logarithmic differential pore-volume distribution (dV/dlogD), which is plotted as a function of pore diameter. Both coated anode Ni-based electrodes

16146840, 0, Downloaded from https://onlinelibrary.wiley.com/doi/10.1002/ænm.202405285 by Dtsch Zentrum F. Luft-U. Raum Fahrt In D. Helmholtz Gemein

, Wiley Online Library on [13/02/2025]. See the Terms

and-conditions) on Wiley Online Library for rules of use; OA articles are governed by the applicable Creative Commons

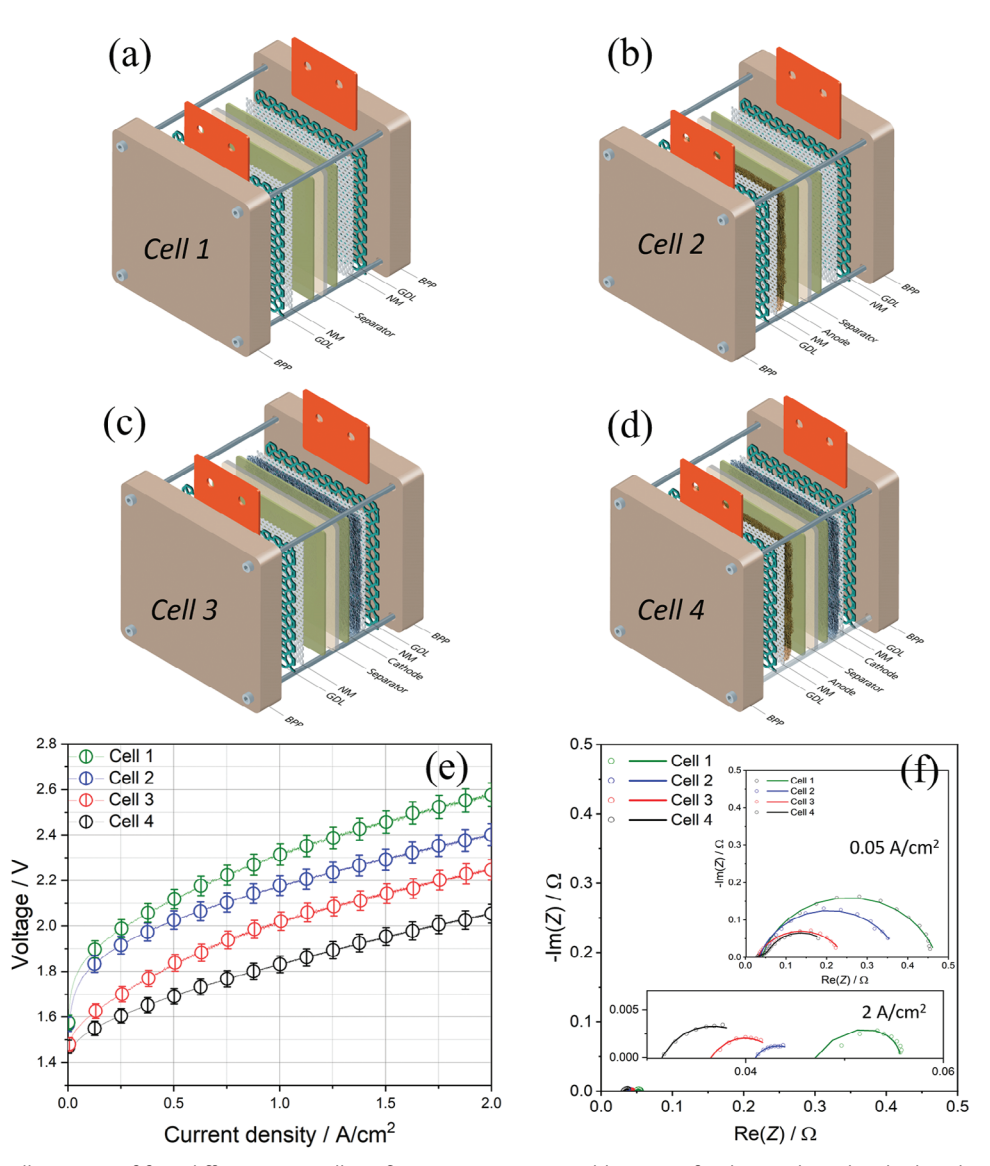


Figure 2. Schematic illustration of four different AWE cell configurations: a) uncoated bare NM for the anode and cathode sides (Cell 1), b) coated Ni-based electrode for the anode side and uncoated bare NM for the cathode side (Cell 2), c) uncoated bare NM as an anode side and coated Mo incorporated porous Ni for the cathode side (Cell 3), and d) coated Ni-based electrode as an anode and coated Mo incorporated porous Ni as a cathode side (Cell 4). Electrochemical characterization of the AWE with different cell configurations in 30 wt.% KOH at 70 °C, e) polarization curves for different Cells 1–4 f) and Nyquist plots from the EIS measurements for different Cells 1–4 at 2 A cm⁻²; the magnified Nyquist plots of different cells at 2 A cm⁻² are shown in the lower inset, while the Nyquist plots of different cells at 0.05 A cm⁻² are shown in the upper inset.

and coated cathode Mo incorporated porous Ni show significant pores in a range from $\approx\!0.01$ to $100\,\mu m$. According to Figure 1c,d, the pore diameter for coated anode Ni-based electrode is located at 0.53 which significantly is dominated by a smaller pore size of 0.31 μm . However, the main pore diameters for coated cathode Mo incorporated porous Ni are larger, located at 1.23 μm , and dominated by a smaller pore size at 0.76 μm . The highly open pore structure and surface area favorably alter the wettability of the electrode and penetration of mass/ions through the electrolyte, facilitating the gas molecule evacuation, especially at higher current densities. $^{[18]}$

Electrochemical characterizations were performed to investigate the influence of NM substrates with low porosity and porous

anode and cathode coatings with different porosity and pore size distributions on the AWE cell performance specifically at high current densities. As can be seen in the schematic illustration in Figure S5 (Supporting Information) and Figure 2a–d, the NM substrate and porous anode and cathode electrodes coated on NM substrate are implemented in the AWE cell assembly to explore the effect of each electrode on the full cell AWE performance.

As Figure 2a–d shows, four different cells with various configurations were assembled placing a commercial Zirfon Perl UTP 500 separator (see the Experimental section) between two uncoated bare NM for the anode and cathode sides (Cell 1), coated Ni-based electrode for the anode side and uncoated bare NM for the cathode side (Cell 2), uncoated bare NM as an anode side and





www.advenergymat.de

coated Mo incorporated porous Ni for the cathode side (Cell 3), and coated Ni-based electrode as an anode and coated Mo incorporated porous Ni as a cathode side (Cell 4). Figure 2e shows the polarization curves of AWE cells for the four different cell configurations, operated at 70 °C in a 30 wt.% KOH. Cell 1 with both sides bare NM substrates delivered the highest cell voltage with 2.57 V at a current density of 2 A cm⁻². However, Cell 4 with both sides coated porous Ni-based anodic electrodes and coated Mo incorporated porous Ni cathodic electrodes delivered the lowest cell potential of 2.05 V at the same current density. Thus, an improvement of ca. 0.52 V for Cell 4 with both sides coated electrodes at 2 A cm⁻² compared with the cell with the uncoated bare NM at both sides was attained. As it is shown in Table \$1 (Supporting Information), this performance is one of the highest performances reported for Raney Ni-based electrodes in alkaline conditions. Other cell configurations with only one side coated electrodes either coated porous Ni-based anodic electrodes (Cell 2) or coated Mo incorporated porous Ni cathodic electrodes (Cell 3) with bare NM electrodes at the other side, delivered a cell potential of 2.4 and 2.24 V, respectively at 2 A cm⁻². As can be seen from the polarization curves in Figure 2e, at high current densities where the ohmic resistance plays an important role, Cell 4 with both sides coated electrodes lowered the cell voltage more significantly than that of Cell 1 with uncoated bare NM across a range of current densities including higher current densities, which is due to the presence of highly active and porous coated electrodes. Cell 3 with coated Mo incorporated porous Ni cathodic electrode but bare NM substrate as an anode lowered the cell voltage more significantly than that of Cell 2 with coated porous Ni-based anodic electrodes and bare NM substrate as a cathode. This can be due to the less sluggish reaction at the cathode side compared to the anode at low current densities and also due to the cathode's higher porosity and larger pore size distribution at higher current densities, which affects bubble formation/removal and consequently reducing ohmic loss. At lower current densities, where the performance is linked to activation loss, the incorporation of Mo to the cathode has been reported to facilitate the hydrogen evolution reaction (HER).[5] This aligns with the results of better performance of Cell 3 compared with Cell 2 and Cell 1 with NM bare substrates as cathodes. First-principles calculations, based on Density Functional Theory (DFT), showed that the incorporation of Mo atoms into Ni-based electrodes enhances the thermodynamics of HER. This is valid at lower current density operations, where the catalytic activity of the electrode species and consequently activation loss is a dominant factor. While the influence Mo on the kinetics of the process remains unclear, it appears to be closely linked to the structure and geometry of the exposed metal surfaces. Detailed results from the DFT calculations are presented in Figures S6-S12 and Tables S2-S4 (Supporting Information). However, at the higher current densities, where the ohmic loss is linked with electrode structures and consequently more effectively bubble removal, the larger pore size and pore size distribution of coated cathode can facilitate diffusion of gases to the flow channel in a direction opposite to the electrolyte flow and more efficiently remove the bubbles when compared to a coated anode specifically at higher current densities.[8] As can be seen from the polarization curves, at lower current densities where the activation loss plays a role, Cell 3 with a coated cathode and bare substrate as anode lower the cell voltage more significantly than that of Cell 2

with a coated anode and bare substrate as a cathode. The performance of these two latter cells is higher than that of the cell with the uncoated bare substrates but lower than that of the cell with coated electrodes at both the anode and cathode sides. These results show that the introduction of both coated anode and coated cathode as electrodes into the cell is necessary for successfully lowering the cell voltage at the whole range of current densities. However, the cathode shows a higher contribution in reducing the voltage at any particular current density, which can be due to high activity due to the less sluggish reaction at the cathode side and the possibility of the cathode being more efficient in removing bubbles and reducing the contact loss due to its highly porous structure with a broad range of micro sizes. This performance improvement across a range of current densities, on a system level, can have a direct and significant impact on the operational expenditure.

The positive effect of the anode and cathode-coated electrodes in the AWE cell was also confirmed by electrochemical spectroscopy (EIS) analysis, which was recorded during in situ fullcell testing. Figure 2f shows the impedance analysis together with their model fits as a Nyquist plot. The equivalent circuit consisted of ohmic resistance R_{ohm} in series with a circuit, comprising a charge transfer resistance for cathode and anode reaction, R, along with their constant phase element in parallel to each other. The R_{ohm} or high-frequency resistance, which appears as the intercept of the Nyquist plots with the x-axis at high frequency (left side of Nyquist plot) represents the total internal ohmic resistance of the cell, which arises mainly from solution and membrane resistance and electrode structure and porosity.[8] R is identified with the cathode and anode activity. The inductor (L) in series with the R_{ohm} is also considered in the model representing possible inductive parts of cables and other components. Figure 2f shows the analysis and comparison of the Nyquist plots with their model fits for all four cells at two different current densities: 0.05 A cm⁻² in the upper inset, and 2 A cm⁻² in the general Figure. The magnified Nyquist plots of all four cells at 2 A cm⁻² are shown in the lower inset of Figure 2f. The impedance data collected at a low current density 0.05 A cm⁻², where the charge transfer resistance R is assigned to the cathode and anode activity and is the most dominant factor for the total cell performance, show that R drastically decreased when NM is replaced by coated anode or coated cathode electrodes. The same trend was also observed for ohmic resistance. However, the effect on R_{ohm} is more visible at higher current densities, where R related to electrode activity influence becomes smaller. The resulting values of charge transfer resistances can be read from low current densities of 0.05 A cm⁻². The values are in the following order: Cell 1 (R: 0.43 Ω) > Cell 2 (R: 0.34 Ω) > Cell 3 (R: 0.21 Ω), Cell 4 (R: 0.19 Ω). The R_{ohm} reduces from 0.039 for Cell 1 to 0.025 for Cell 4. However, to see the direct effect of electrodes on the ohmic resistance of cells, the impedance should be recorded at a higher current density of 2 A cm⁻², where the ohmic resistance is the most dominant factor for the total cell performance. Figure 2f and its magnified image in the lower inset show that the ohmic resistance decreased when NM is replaced by coated anode or coated cathode respectively. However, the effect was more prominent when NM at the cathode side was replaced by the coated cathode. The values of ohmic resistance at a high current density of 2 A cm⁻² are in the following order: Cell 1 ($R_{\rm ohm}$: 0.04 Ω) > Cell 2 ($R_{\rm ohm}$: 0.034 Ω)

16146840, 0, Down loaded from https://onlinelibrary.wiley.com/doi/10.1002/ænm.202405285 by Dtsch Zentrum F. Luft-U. Raum Fahrt In D. Helmholtz Gemein.

Wiley Online Library on [13/02/2025]. See the Terms and Conditions (https://onlinelibrary.wiley.com/terms-and-conditions) on Wiley Online Library for rules of use; OA articles are governed by the applicable Creative Commons

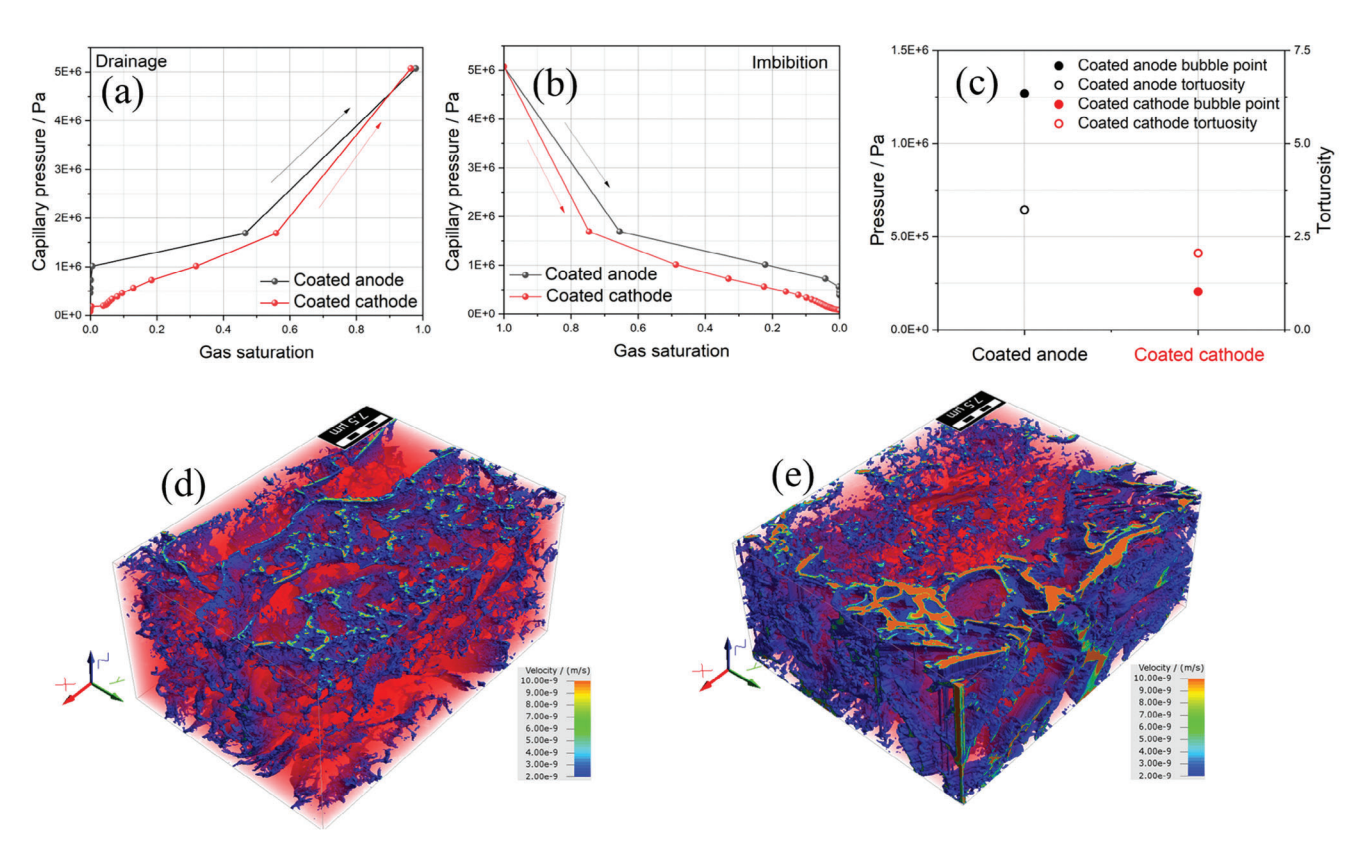


Figure 3. Simulation of a) drainage and b) imbibition for the coated anode and coated cathode (coated porous Ni-based anodic electrode and coated Mo incorporated porous Ni cathodic electrode). c) Calculated bubble point and tortuosity for the coated anode and coated cathode. Saturation and flow simulation of coated electrodes. Simulated water flows through the FIB-SEM-measured structure of d) coated anode, coated porous Ni-based anodic electrode, and e) coated cathode, coated Mo incorporated porous Ni cathodic electrode.

> Cell 3 ($R_{\rm ohm}$: 0.03 Ω), Cell 4 ($R_{\rm ohm}$: 0.027 Ω). Ohmic resistance in addition to the conventional Zirfon separator resistance is also affected by the structure of the electrodes and the formation and removal of gas bubbles. Therefore, since all the cells use the same separator and cell components, the change in the ohmic resistance can be attributed to the coated electrode structures and a better liquid/gas flow. However, the coated cathode with more appropriate pore size distribution and higher porosity compared to those of the coated anode can reduce the trapped-bubble concentrations between the Zirfon and electrode surface, which leads to a further decrease of ohmic resistance and in turn can contribute to an increase of the overall cell performance. However, the porous coated anode electrode is still more efficient than the bare NM substrate in reducing the total cell resistance including ohmic resistance, and increasing overall performance. Therefore, the incorporation of both coated anodic and cathodic in Cell 4 shows the lowest cell resistance including ohmic resistance, and consequently higher cell performance.

To further investigate the contribution of the coated components on the performance of the electrolytic cells, FIB-SEM 3D data were acquired and processed with GeoDict. Several modules of GeoDict were used to describe the structure and to highlight their influence on water electrolysis. Possible explanations for the two-phase gas/liquid flow behavior of the porous electrodes may be found through comparing the morphology of these throughplane paths for coated electrodes. The size of the pores can be de-

scribed by the calculation and visualization of the Euclidian distance. In Figure \$13a,b (Supporting Information) the calculated map of the Euclidian distances for the coated porous Ni-based anodic electrode and the coated Mo incorporated porous Ni cathodic electrode, respectively, are shown and the larger pores of the cathodic electrode are clearly visible.

The uptake and release of electrolytes for a given porous medium can be described by capillary pressure curves. The results of the simulated drainage and imbibition (water uptake) of the coated anode and coated cathode are shown in Figure 3a,b, respectively. Concerning water extrusion (drainage), the cells with coated Ni-based electrode anode, show a steeper slope compared to cells with the coated Mo incorporated porous Ni cathode, suggesting that more pressure is needed to press water out in the case of gas penetration from the electrode side. [43] The shift of the curve for the coated anode to the higher values can be attributed to lower permeability when compared to the coated cathode. This is the case for both the drainage and the imbibition (water uptake) curves. These observations explain the relatively lower performance of the cell with anodic anodic-coated electrode due to the high pressure necessary for transporting gases through the small pores. Regarding the imbibition, the results also show steeper slopes, suggesting that water uptake is more efficient. Upon investigating the complexity of through-plane pathways, the cells with coated porous Ni-based anodic electrode show exceptionally higher tortuosity than those with coated Mo incorporated porous

6146840, 0, Downloaded from https://onlinelibrary.wiley.com/doi/10.1002/aenm.202405285 by Dtsch Zentrum F. Luft-U. Raum Fahrt In D. Helmholtz Gemein.

"Wiley Online Library on [13/02/2025]. See the Terms and Conditions (https://onlinelibrary.wiley.

and-conditions) on Wiley Online Library for rules of use; OA articles are governed by the applicable Creative Commons

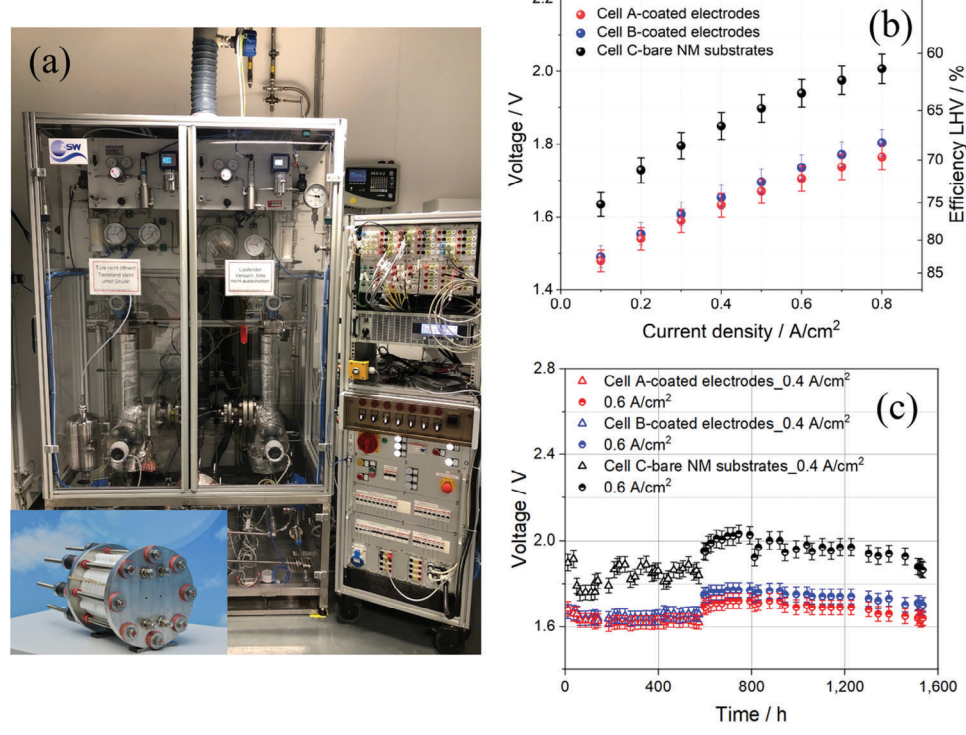


Figure 4. a) Photo of the AWE test bench, inset is a photograph of the utilized a 2 kW stack, b) polarization curves for different cells of 2 kW stack of, cell C with bare NM substrates and cell A and B, two cells with coated electrodes at both sides (coated porous Ni-based anodic electrode and coated Mo incorporated porous Ni cathodic electrode) at 70 °C in 30 wt.% KOH, c) a durability test at two different current densities of 0.4 and 0.6 A cm⁻² (in total with a duration of 1534 h) at 70 °C in 30 wt.% KOH for different cells of the stack, cell A, cell B and cell C.

Ni cathodic electrode; this suggests that the pathways that gas and water have to traverse are longer in the anode. Porous structures and their efficiency for electrolysis can be described by branching in the pores. Generally speaking, the geometric tortuosity τ_{α} can be described as the ratio of the flow path given by the porous medium to the ideal straight path without the medium, with an ideal flow path achieving a tortuosity of 1.[44] The tortuosity of the through-plane pores was calculated using the module the Diffu-Dict module within GeoDict. As shown in Figure 3c, τ_g of the coated anode with 3.17 is much larger than τ_{α} of the coated cathode material with 2.02. The calculated tortuosity factor for air described via Knudsen diffusion is significantly lower for the cathodic electrode (4.06) than the anodic electrode (10.02) and expresses the reduction of the effective diffusivity due to the actual pore shape of the electrode medium. Another important property to describe the pores in a porous medium is the bubble point. The bubble point is defined as the minimum gas pressure needed to force the electrolyte out of the medium.^[4] The bubble point is significantly lower for the cathodic electrode. The calculated tortuosity and bubble points are presented in Figure 3c. For comparison, a synthetic structure for bare substrate was generated with GeoDict (for more details see Experimental part), Figure \$14 (Supporting Information). Due to the low porosity of the substrate, no continuous paths were found through the material, so that a calculation of the bubble point and tortuosity is not possible for the bare substrate. The pressure that would be necessary to remove a liquid from the pores is therefore close to infinity, as is the tortuosity. Therefore, both tortuosity and bubble point can be expected to be

much lower for coated electrodes than bare substrates. An estimation of the electrolyte flow through the electrodes was made by simulating the flow of water through these structures. Comparative simulation of water mass flow rates through the porous media was undertaken using the GeoDict module FlowDict. The connected areas and the paths of the mass flow are visually represented as the resulting water flow velocity for the coated anode and coated cathode in Figure 3d,e. These simulations show a higher proportion of paths participating in the electrolyte flow for the coated cathode leads to From the electrochemical results, the coated cathode has a more positive influence on the performance at all ranges of current densities. The higher porosity of the coated cathode leads to a higher number of connected channels and, hence, a higher velocity in the channels. These findings are in good agreement with the polarization curves in Figure 2e.

To validate the functionality of the non-precious thermal coated electrodes in terms of performance and durability, using an AWE system test bench, **Figure 4a**, the 100 cm² anodic and cathodic electrodes are implemented in a 2 kW stack (inset of Figure 4a). In Figure 4b, examples of polarization curves for three cells, cell A and cell B (with coated electrodes at both sides, coated porous Ni-based anodic electrode, and coated Mo incorporated porous Ni cathodic electrode) and cell C (with bare NM substrates for both anodic and cathodic sides), are recorded at 70 °C in 30 wt.% KOH up to 0.8 A cm². It can be seen that cell C with bare NM substrates as electrodes delivered the highest cell voltage with 2.0 V at a current density of 0.8 A cm². However, cell A and cell B with coated electrodes at both sides delivered a



ADVANCED ENERGY MATERIALS

www.advenergymat.de

lower potential of 1.76-1.8 V at the same current density, which is close to the results obtained from the single cell. This shows that these electrodes can be successfully scaled up to achieve high performance for industrial AWE applications. It was not possible to record data at higher current densities in the stack due to the limited range of the power supply. The voltage reduction translates as an efficiency increase from 61.2 LHV% for the cell of the stack with NM bare substrates, cell C, to 68.1-69.7 LHV% for the cells of A and B of the stack with coated electrodes as anode and cathode at the highest current density. This efficiency improvement, on a system level, can have a direct and significant impact on operational expenditure. These results show that the introduction of coated electrodes as the anode and cathode sides (coated porous Ni-based anodic electrode and coated Mo incorporated porous Ni cathodic electrode) into the cells of the stack can effectively lower the cell voltage and increase the efficiency across a range of current densities. Extrapolating from the results obtained in this work to market demands, the cost reduction of green H₂ can be significant. Depending on the particular application and operation strategies, feeding power from renewable energy into the existing grid, brings challenges, requiring a performance optimization in terms of efficiency, current density, and partial load as well as significant investment cost associated with AWE operating at GW capacity. The low current density negatively impacts system size and H₂ production costs. The cost of stack components scales with the geometrical electrode area, while the amount of produced H₂ is proportional to the current. Therefore, the possibility of operation at a much higher current density while maintaining cell efficiency could not only reduce the effective costs of the electrochemical stack by reducing the stack size but also increase the amount of H₂ production. Higher H₂ production that allows for a reduction of stack size is needed to cut production costs and bring green H2 into the energy mainstream. One crucial challenge that may arise is the long-term stability of the AWE stack with thermally coated electrodes. To address this, the voltage/time characteristics of stacks with both sides using coated electrodes at (cell A and cell B) and also with bare NM substrates (cell C) are recorded at two different current densities of 0.4 and 0.6 A cm⁻², each for 573 and 961 h, respectively. Encouragingly, the cell voltage at 0.4 and 0.6 A cm⁻² after 1534 h of continued operation shows almost no performance degradation. This suggests that the thermally sprayed electrodes are highly robust against the examined harsh operational conditions, which could make them a suitable and excellent candidate for long-term industrial use.

After the durability test, the samples were subjected to X-ray photoelectron emission spectroscopy (XPS), XRD, and EDX analysis to determine the changes in phase and elemental composition. For comparison, XPS was also carried out for fresh activated coated samples as well. The detailed spectra of the nickel 2p_{3/2} regions of the investigated electrode surfaces, plotted in Figure S15a,b (Supporting Information), show the differences in chemistry of the nickel components for fresh-coated electrodes and aged ones. The electrodes before operation exhibit for both anodic and cathodic electrodes two additional signals at 852.5 and 854.0 eV, which can easily be attributed to metallic nickel and nickel (II) oxide and distinguished from the nickel hydroxide signals at >855 eV present in all samples.^[45] Uniformly, after aging the coated anode and the coated cathode electrodes show

no nickel metal and low nickel oxide. The slightly asymmetric peak shape of the aged sample suggests the presence of a small amount of NiO (indicated at ≈854 eV); however, the peak fitting procedure did not conclusively converge, so the spectral data are not unambiguously clear. It should be noted that the information depth of this method is in the one-digit nanometer range. However, after degradation, both samples still consist of a floating mixture of NiOOH and Ni(OH), with a broad composite peak as described elsewhere and also a small amount of NiO.[45] The detailed spectra of the Mo3d region of the coated cathodic electrode (Figure S15c, Supporting Information) show a similar behavior. The pristine electrode coating exhibits three different Mo components, metallic Mo at 227.8 eV and the two higher oxidation states Mo(+IV) at 230.2 eV and Mo(+VI) at 232.6 eV for the Mo3d_{3/2} signal each, while the aged electrode shows the latter only. [46] The lower oxidation state compounds of the freshly activated electrodes are completely turned over to Mo(+VI), most probably MoO₃, and Ni(OH), and NiOOH, which cannot be conclusively separated by means of this analysis method. As can be seen in Figure S16a,b (Supporting Information), the XRD pattern of the coated anode electrode and coated cathode electrode after durability test still keep the same pattern as the fresh activated samples as Figure S1 (Supporting Information) but with the appearance of new peaks which is reported to be indication of a slight presence of Ni oxide and hydroxide in the case of coated anode based on porous Ni and also Mo in oxide forms in the case of coated cathode based on Mo incorporated porous $\mathrm{Ni.^{[47-57]}}$ The increase of blue color related to oxygen in EDX analysis for both coated anode and cathode electrodes after aging can be due to the formation of hydroxide and oxides on the electrode surface during the long continuous operation in highly KOH solution (Figure S16c-f, Supporting Information).

Hydrogen permeation is an important phenomenon for AWE, due to several reasons related to safety issues and efficiency loss. Figure \$17 (Supporting Information), shows the time evolution of the H₂ in O₂ content when holding the stack at 0.4 A/cm² \approx 400 h. The H_2 in O_2 contents at the beginning of the test (BOT) is 0.75 vol.%, which stays constant over the duration of ≈400 h by the end of the test (EOT), showing that stack has almost constant H2 in O_2 content over time of operation at a constant current density This also satisfies a chosen safety limit of 2 vol.% H₂ in O₂, which is about half the extent of the previously mentioned lower explosion limit (LEL) of ≈ 4 vol.% H₂ in O₂ [58] The stack also exhibits an insignificant and negligible presence of O2 at the beginning of the test (BOT) (0.14 vol.%), which stays constant over \approx 400 h of operation. This exhibit showcases the compatibility between electrode and diaphragm, emphasizing their seamless integration and their ability to work together harmoniously with the absences of any detrimental effects on the diaphragm causing gas crossover.

3. Conclusion

Currently, all research efforts in AWE have primarily focused on improving performance at higher current densities by reducing ohmic resistance using alkaline membranes instead of conventional diaphragm. In contrast, this research effort examined the effect of Raney Ni-based electrodes' porosity and their pore size distribution on ohmic resistance associated with the evolution



www.advenergymat.de

of bubbles and, consequently, the performance of AWE at high current densities. The results indicated that low tortuosity and low bubble point of the electrodes, influenced by electrode structure, are critical for efficient mass transfer during the electrolysis operation at high current densities. To better understand the impact of electrode porosity, several physical characteristics, such as bubble point and tortuosity were correlated with the polarization curves. The results showed that the electrodes with higher porosity and larger pore size more efficiently reduced the total resistance. High porosity, broad pore-size distribution, and low tortuosity of cathodic electrodes reduce capillary pressure in the forms of drainage and imbibition facilitating gas bubble removal formed at the electrode surface more efficiently compared to the anodic electrode with lower porosity and smaller pores. The results of simulating the water flow through the structure suggest that the larger pores might ensure higher mass transport and result in lower bubble point, whereas smaller pores may drive bubble formation outside the electrodes and, thus, away from the catalytic surface, enabling continuous electrochemical reactions and an effective two-phase flow. On the other hand, DFT calculations revealed that the incorporation of Mo atoms into Ni-based electrodes enhances the thermodynamics of HER. However, this effect is predominantly valid at lower current density operations, where the catalytic activity of the electrode is critical, and activation losses are the primary performance-limiting factor. A combination of both coated anodic and cathodic porous electrodes (coated porous Ni-based anodic electrode and coated Mo incorporated porous Ni cathodic electrode) in the cell leads to a high current density of 2 A cm⁻² at ≈2 V compared with the cell with bare NM substrates as electrodes with very low porosity. The performance and durability of coated electrodes in combination with Zirfon is validated in a 2 kW stack, demonstrating the high performance of 1.76 at 0.8 A cm⁻² with no degradation at constant current densities of 0.4 and 0.6 A cm⁻² in total for 1534 h.

4. Experimental Section

Electrode Preparation and Characterization: Electrodes were produced by spraying globular gas-atomized Nickel-Aluminum type alloy powders with and without Mo for anode and cathode electrodes, respectively. Al acts as a pore-forming agent. Coated porous electrodes were produced on the surface of 4 cm² Ni mesh (NM) substrate using a thermal spray technique. For this, Ar with secondary gases was used. [8,34,59] The spray powder was injected through external injection nozzles into the plasma jet, where particles were accelerated and heated due to momentum and heat transfer between plasma and particles and the quasi or fully molten particles impacted the substrate surface, flattened, solidified, and consolidated to form an electrode coating on top of NM substrate. Before the electrochemical test, the electrodes were activated in 30 wt.% KOH with a suitable complex former for removing Al as a pore-forming agent to form porosities.^[34,59] Electrode characterization and numerical simulation: XRD patterns of the coating samples were acquired using an X-ray diffractometer STADI P (STOE, Germany). SEM and EDX were done on resin-embedded and polished samples using a Zeiss Gemini Ultra plus microscope. The chemical compositions of the samples were determined by the EDX spectrometer/detector from the Bruker company. In order to prepare the sample for the FIB-SEM procedure, the electrodes were mechanically cut into smaller pieces of 5 mm x 5 mm for better stability during the high tilt in the tool. Subsequently, the sample was glued on an aluminum sample holder using silver conductive RS glue with the cathode layer facing on top. Slicing of the electrode was done by ion milling (Ion beam cutting) using gallium (Ga+) as the ion source. All cross-sections were subsequently made with a focused Ga+ beam at an accelerating voltage of 30 kV and a current of 500 nA. Each cross-sectional cut was made at a distance of 25 nm between each section in the z-direction. Consecutive imaging of serial sections was acquired by FEG-SEM at a set magnification of 4000 x with an additional reduced area focusing on the area of interest. All images were obtained at an acceleration voltage of 5 kV with the In-lens detector. For the electrodes discussed later, 240 FIB slices were prepared. The 240 consecutive SEM images, with a resolution of 27.9 nm (along x) x 27.9 nm (along y) x 50 nm (along z, since every second slice was documented) for electrodes were then analyzed by different software applications for further information. A custom-built MATLAB was used for image segmentation purposes. It was important to note that the FIB-SEM raw pictures are shown in grayscale images in which the darker parts refer to the pores and the brightest ones correspond to the solid matrix. The porosity measurements of the samples have been performed by MIP (Pascal 140/240, Thermo Scientific up to a pressure of 200 MPa). MIP involves forcing mercury into the pores of samples by the application of a pressure to measure the size and volume of pores. As pressure was applied, mercury fills the larger pores first. As pressure increases, the filling proceeds to smaller pores. The pore-size distribution was determined from the volume intruded at each pressure increment. The pore-size distribution was represented as cumulative pore volume and the first derivative of the cumulative curve, dV/dlogD as a function of pore diameter. For the purpose of simulating the properties of the porous electrodes GeoDict software (Math2Market GmbH) was used. Bubble point and capillary pressure curves were obtained using the structures from FIB-SEM measurements for both coated cathode and anode. In these relatively small area measurements compared to other techniques, the pores were quite small, and as these properties (bubble point and capillary pressure curves) were directly related to the maximum pore size in the area used for simulation. The segmented FIB-SEM images of the measured structures were imported using the built-in Import Geo-Vol module. The edges of the images were cut to remove of clearly visible artifacts from FIB cutting. The imported images resulted in a 3D model of the electrodes which was used for further analysis with different modules of GeoDict. The SatuDict module was used to calculate the capillary-pressure curves for the given structures for imbibition and drainage processes. Wetting and nonwetting phase reservoirs were added in z+ and z- directions, respectively. The capillary-pressure curves were acquired using a contact angle of \approx 29°. [60] From the obtained results of the capillary-pressure curves, the relative permeability and diffusivity were calculated. For receiving the geometric tortuosity factor Knudsen diffusivity simulations were conducted on both structures using the module DiffuDict with air as fluid. The porosity of the given structure divided by the resulting effective diffusivity from the simulations gives the tortuosity. The module FlowDict was used to calculate the flow through the structure using the Navier–Stokes–Brinkman equations by adding in- and out-flow regions. PoroDict within GeoDict was used to calculate the pore-size distribution and to visualize open and closed porosity. Using the MIP data from the bare substrate a synthetic structure was generated using the pore size distribution and generating the pores as grains in an empty space. The structure was then inverted resulting in a solid structure with the generated grains as pores. The surface chemistry was investigated with X-ray XPS in a vacuum system with a base pressure of 2×10^{-10} mbar, using a monochromated Al Klpha source with an X-ray energy of 1486.^[61] 74 eV and a hemispherical analyzer (ESCALAB Xi+, FEI / ThermoFisher Scientific). The peak shape analysis was carried out with Unifit 2016, applying convoluted Gaussian/Lorentzian profiles and a Shirley background function. [62] The surface stoichiometry of the occurring atoms/signals was calculated using the numerically fitted peak areas, photoionization cross sections by Yeh and Lindau, [63] and instrumental transmission functions given by the manufacturer. The energy axis of the system was calibrated by means of Au4f, Ag3d, and Cu2p signals of the corresponding ion-etched reference metals. The elemental composition, focusing only on the electrode metals and ignoring other adventitious elements, averaged over two or, respectively, three samples. Electronic structure simulations of the different structures were performed using ab initio methods within the DFT.^[64,65] The calculations were performed through the VASP code (Vienna ab initio Simulation Package). [66-70] The projector augmented wave (PAW) method, [70,71] was employed in order to

ADVANCED SCIENCE NEWS

www.advancedsciencenews.com



www.advenergymat.de

account for the electron-ion core interaction, utilizing the GGA (Generalized Gradient Approximations) exchange-correlation functional with the PBE parameterization (Perdew-Burke-Ernzerhof). [72,73] PAW-PBE potentials with the following valence electrons: Ni (3s²3p⁶ 4s²3d⁸), Mo (3s²3p⁶ $4s^23d^{10}4d^55s^1$), O $(2s^22p^4)$ and H $(1s^1)$ were used. The k-space grid sampling used for the surfaces model was 5×5×1 and a cut-off energy for the plane wave expansion of 499 eV was selected in all the calculations. For the simulation, a vacuum space of 15Å was selected in concordance with early works in the non-periodic directions to prevent periodic image-to-image interaction; this vacuum was successfully used in previous works. [74,75] The structure was optimized until the forces in all the atoms were lower than 0.01 eV/Å, and the unit cell was optimized until the components of the stress tensor were lower than 1 kBar. Dispersion correction terms in total energy were included by means of the Grimme, [76] method with Becke-Johnson damping function.[77] Phonon analysis, by means of finite size displacement, was applied for adsorbed H₂O and OH* and H* on different surfaces. It allows the estimate zero-point energy corrections. Nudged elastic band (NEB) calculations were applied to find and confirm transition states between molecular and dissociated water upon Ni and Ni₃Mo on surfaces (111) and (100) surfaces. In all the cases the most favorable molecular adsorbed sites and dissociated systems were taken as the starting and final points, considering five NEB images in between. An RMM-DIIS algorithm was selected with a spring constant of -5 eV/Å between each image to find the transition state. Each was confirmed with vibrational frequency calculations as having a single imaginary frequency. Finally, initio Molecular Dynamics assisted with Machine-Learning force fields (MLFF-AIMD) as implemented in VASP was conducted to map the configurational space, considering the initial and final structures utilized in the NEB calculations. In reference to the simulation cell, a $2\times2\times1$ supercell is built to increase four times the degree of freedom in comparison to the early set-up. The MLFF-AIMD simulation included the Nose-Hoover NVT ensemble at T = 300 K with a time step of $\Delta t = 0.1 \, fs$ with total simulation time ranging between $t_f = 1.0$ and 2.4 ps, depending on the considered case.

AWE cell Electrolyzer Test: The zero-gap electrolyzer cell consists of five main parts: nickel bipolar plates, Ni wire mesh as gas diffusion layers (GDL), Zirfon PERL UTP 500 separator and NM substrate and porous Ni electrodes, coated Ni-based electrode as anode and coated Mo incorporated porous Ni as cathode. Zirfon was placed between two electrodes and supported from each side by porous Ni GDLs and fixed by Nickel bipolar plates from both sides. Four different cells with various configurations were assembled placing a commercial Zirfon Perl UTP 500 separator between two uncoated bare NM for the anode and cathode sides (Cell 1), coated Ni-based electrode for the anode side and an uncoated bare NM for the cathode side (Cell 2), uncoated bare NM as an anode side and coated Mo incorporated porous Ni for the cathode side (Cell 3), and coated Nibased electrode as an anode and coated Mo incorporated porous Ni as a cathode side (Cell 4). The test was done at atmospheric pressure in 30 wt.% KOH at 70 °C, by recording polarization curves up to 2 A cm⁻² with a scan rate of 10 mA s $^{-1}$, after 30 min activation at a constant current of 0.2 A using a potentiostat from biologic. EIS was performed at low and high current densities from 100 kHz to 100 mHz to identify the losses. The operating conditions and cell hardware were kept the same for all the tests. The equivalent circuit for fitting consisted of lumped resistance (Rohm) in series with a circuit, comprising a charge transfer resistance including both cathode and anode charge transfer resistance (R) along with their constant phase element in parallel to each other. However, an additional charge transfer resistance in parallel to a constant phase element had to be added for fitting impedance spectra of Cell 4 at low current densities, as anodic and cathodic contribution possess relaxation times of different magnitudes and hence appear as two processes in the recorded impedance response. Therefore, the sum of the anodic and cathodic charge transfer resistance was reported as the total charge transfer resistance for this cell. The inductor (L) in series with the R_{ohm} represents possible inductive parts of cables and other components. The fitting of the Nyquist plot was done by RelaxIS3 software from rhd instruments. For the Nyquist plot fitting, the effect of a high-frequency tail extending toward positive imaginary parts, which was considered to be inductive contributions due to the electronics

and wires was included. However, at very low frequencies significant residuals were observed. The residuals were scattered randomly in the positive and negative directions, which suggested that they were caused by noise. As this noise becomes dominant, fitting was no longer possible in this frequency range. This holds true, especially for higher current densities where parasitic impacts become even more pronounced.

Stack Electrolyzer Test: It was performed on a 2 kW-stack. The cell assembly consisted of two electrode packages each consisting of stainlesssteel bipolar plates, two stainless steel current collectors, and a pair of electrodes (coated porous Ni-based anodic electrode and coated Mo incorporated porous Ni cathodic electrode or only bare NM substrates as electrodes), sandwiching a Zirfon UTP 500 diaphragm in a zero-gap configuration. The stack was maintained as a closed and hermetically sealed environment. To prevent the reaction of KOH with atmospheric CO2 and the subsequent formation of carbonate salts, the demi water undergoes continuous purging with nitrogen, ensuring an inert atmosphere and complete isolation from the air. The cell voltage was directly measured at the electrodes to avoid influences of contact resistance at the current collector and the bipolar plate, affecting the measurements and thus increasing the comparability of electrode performance. The piping and instrumentation diagram (P&ID) of the test bench for 100 cm² stack measurements is illustrated in Figure \$18 (Supporting Information). The setup includes two separate electrolyte cycles, each equipped with a pump, followed by a flow measurement system and sensors to monitor the inlet and outlet temperature of the stack. Pressure was measured in both separators and the temperature of the electrolyte was controlled using heaters surrounding each separator. Demi water supply was provided only to the hydrogen separator. The quality of the product gases was assessed after they were dried, ensuring accurate measurement. The system was controlled using software programmed on NI LabViewTM. Polarization curves were measured from 100 to 800 mA cm⁻² in 100 mA cm⁻² steps while holding each step for 60 s for stabilization of the measurement. For long time duration degradation testing the stack was operated at a current density of 0.4 A cm⁻² for \approx 573 h followed by operation at 0.6 A cm⁻² to complete a 1534 h test run. The rectifier used for operating the stack was a PS9040-170 from EA Elektro-Automatik.

Supporting Information

Supporting Information is available from the Wiley Online Library or from the author.

Acknowledgements

This project has received funding from the German project BW-Elektrolyse ("Elektrolyse made in Baden—Württemberg", Ministry of Economic Affairs in Baden—Württemberg), H2Giga-Degrad EL3, and European Union's Horizon 2020 research and innovation program under grant agreement No. 862509 ("NEXTAEC"). RF, and LFW, and ME wish to thank the Uruguayan CSIC, ANII, and PEDECIBA funding institutions. Computational work performed at the Center for Nanoscale Materials, a U.S. Department of Energy Office of Science User Facility, was supported by the U.S. DOE, Office of Basic Energy Sciences, under Contract No. DE-AC02-06CH11357.

Open access funding enabled and organized by Projekt DEAL.

Conflict of Interest

The authors declare no conflict of interest.

Data Availability Statement

The data that support the findings of this study are available from the corresponding author upon reasonable request.

onlinelibrary.wiley.com/doi/10.1002/ænm.202405285 by Dtsch Zentrum F. Luft-U. Raum Fahrt In D. Helmholtz Gemein/

, Wiley Online Library on [13/02/2025]. See the Terms

and Conditions (https://onlinelibrary.

s) on Wiley Online Library for rules of use; OA articles are governed by the applicable Creative Commons



Keywords

alkaline water electrolysis, bubble point, high current density, hydrogen

Received: November 12, 2024 Revised: January 13, 2025 Published online:

- [1] IEA, Global Energy Review: CO2 Emissions in 2021, International Energy Agency (IEA), 2022, https://www.iea.org/reports/global-energy-review-co2-emissions-in-2021-2.
- [2] United Nations Climate Change, Rise in greenhouse gas concentrations jeopardizes Paris agreement temperature targets, October 2021.
- [3] Mission 2020, https://mission2020.global/(accessed: July 2020).
- [4] S. Stiber, H. Balzer, A. Wierhake, F. J. Wirkert, J. Roth, U. Rost, M. Brodmann, J. K. Lee, A. Bazylak, W. Waiblinger, A. S. Gago, K. A. Friedrich, Adv. Energy Mater. 2021, 11, 2100630.
- [5] S. H. Park, D. T. To, N. V. Myung, Appl Catal a-Gen 2023, 651, 119013.
- [6] X. Pang, J. T. Davis, A. D. Harvey, D. V. Esposito, *Energy Environ. Sci.* 2020, 13, 3663.
- [7] F. Razmjooei, A. Farooqui, R. Reissner, A. S. Gago, S. A. Ansar, K. A. Friedrich, ChemElectroChem 2020, 7, 3951.
- [8] F. Razmjooei, T. Morawietz, E. Taghizadeh, E. Hadjixenophontos, L. Mues, M. Gerle, B. D. Wood, C. Harms, A. S. Gago, S. A. Ansar, K. A. Friedrich, *Joule* 2021, 5, 1776.
- [9] X. Yan, J. Biemolt, K. Zhao, Y. Zhao, X. Cao, Y. Yang, X. Wu, G. Rothenberg, N. Yan, Nat. Commun. 2021, 12, 4143.
- [10] L. Yu, Q. Zhu, S. Song, B. McElhenny, D. Wang, C. Wu, Z. Qin, J. Bao, Y. Yu, S. Chen, Z. Ren, Nat. Commun. 2019, 10, 5106.
- [11] H. Shi, Y.-T. Zhou, R.-Q. Yao, W.-B. Wan, X. Ge, W. Zhang, Z. Wen, X.-Y. Lang, W.-T. Zheng, Q. Jiang, Nat. Commun. 2020, 11, 2940.
- [12] K. Bareiß, C. de la Rua, M. Möckl, T. Hamacher, Appl. Energy 2019, 237, 862.
- [13] S. Kumari, R. T. White, B. Kumar, J. M. Spurgeon, *Energy Environ. Sci.* 2016, 9, 1725.
- [14] T. R. Ayodele, J. L. Munda, Int. J. Hydrog. Energy 2019, 5, 17669.
- [15] H. Zhao, D. Lu, J. Wang, W. Tu, D. Wu, S. W. Koh, P. Gao, Z. J. Xu, S. Deng, Y. Zhou, B. You, H. Li, Nat. Commun. 2021, 12, 2008.
- [16] G. Matute, J. M. Yusta, L. C. Correas, Int. J. Hydrog. Energy 2019, 44, 17431.
- [17] J. Brauns, T. Turek, Processes 2020, 8, 248.
- [18] J. Bleeker, C. van Kasteren, J. R. van Ommen, D. A. Vermaas, Int. J. Hydrogen Energy. 2024, 57, 1398.
- [19] 2020, Hydrogen Europe, October, https://hydrogeneurope.eu/wp-content/uploads/2021/11/Clean-Hydrogen-Monitor-2020.pdf (accessed: October 2020).
- [20] A. Van Wijk, J. Chatzimarkakis, Green Hydrogen for a European Green Deal – A 2×40 GW Initiative 2020, Hydrogen Europe 2020-04-01_Dii_Hydrogen_Studie2020_v13_SP.pdf (dii-desertenergy.org),
- [21] European Commission, Europe, Q&A: A Hydrogen Strategy (europa.eu), 2020.
- [22] O. Schmidt, A. Gambhir, I. Staffell, A. Hawkes, J. Nelson, *Int. J. Hydrog. Energy* 2017, 42, 30470.
- [23] M. Schalenbach, A. R. Zeradjanin, O. Kasian, S. Cherevko, K. J. Mayrhofer, Int. J. Electrochem. Sci. 2018, 13, 1173.
- [24] J. W. Haverkort, H. Rajaei, J. Power Sources 2021, 497, 229864.
- [25] Y. Leng, G. Chen, A. J. Mendoza, T. B. Tighe, M. A. Hickner, C.-Y. Wang, J. Am. Chem. Soc. 2012, 134, 9054.
- [26] T. Kou, S. Wang, R. Shi, T. Zhang, S. Chiovoloni, J. Q. Lu, W. Chen, M. A. Worsley, B. C. Wood, S. E. Baker, E. B. Duoss, R. Wu, C. Zhu, Y. Li, Adv. Energy Mater. 2020, 10, 2002955.

- [27] M. Carmo, D. L. Fritz, J. Mergel, D. Stolten, Int. J. Hydrog. Energy 2013, 38, 4901.
- [28] H. A. Miller, K. Bouzek, J. Hnat, S. Loos, C. I. Bernäcker, T. Weißgärber, L. Röntzsch, J. Meier-Haack, Sustain. Energy Fuels 2020, 4 2114
- [29] S. F. Amireh, N. N. Heineman, P. Vermeulen, R. L. Garcia Barros, D. Yang, J. van der Schaaf, M. T. de Groot, J. Power Sources 2023, 560, 232629.
- [30] C. Karacan, F. P. Lohmann-Richters, G. P. Keeley, F. Scheepers, M. Shviro, M. Müller, M. Carmo, D. Stolten, Int. J. Hydrogen Energy 2022, 47, 4294.
- [31] D. D'Arc de Fatima Palhares, L. Gustavo Martins Vieira, J. J. R. Damasceno, Int. J. Hydrog. Energy 2018, 43, 4265.
- [32] H. Zhou, F. Yu, Q. Zhu, J. Sun, F. Qin, L. Yu, J. Bao, Y. Ying, S. Chen, Z. Ren, Energy Environ. Sci. 2018, 11, 2858.
- [33] M. T. de Groot, A. W. Vreman, *Electrochim. Acta* 2021, 369, 137684.
- [34] M. Luthfi Akbar Trisno, A. Dayan, S. J. Lee, F. Egert, M. Gerle, M. Rykær Kraglund, J. O. Jensen, D. Aili, A. Roznowska, A. Michalak, H. S. Park, F. Razmjooei, S.-A. Ansar, D. Henkensmeier, *Energy Environ. Sci.* 2022, 15, 4362.
- [35] F. Razmjooei, K. P. Singh, D. S. Yang, W. Cui, Y. H Jang, J.-S. Yu, ACS Catal. 2017, 7, 2381.
- [36] K. P. Singh, C.-H. Shin, H.-Y. Lee, F. Razmjooei, A. Sinhamahapatra, J. Kang, J.-S. Yu, ACS Appl. Nano Mater 2020, 3, 3634.
- [37] M. Görlin, J. H. Stenlid, S. Koroidov, H.-Y. Wang, M. Börner, M. Shipilin, A. Kalinko, V. Murzin, O. V. Safonova, M. Nachtegaal, A. Uheida, J. Dutta, M. Bauer, A. Nilsson, O. Diaz-Morales, *Nat. Commun.* 2020, 11, 6181.
- [38] A. Peugeot, C. E. Creissen, D. Karapinar, H. N. Tran, M. Schreiber, *Joule* 2021, 5, 1281.
- [39] M. Gong, D.-Y. Wang, C.-C. Chen, B.-J. Hwang, H. Dai, Nano Res. 2016, 9, 28.
- [40] R. Zahra, E. Pervaiz, M. Yang, O. Rabi, Z. Saleem, M. Ali, S. Farrukh, Int. J. Hydrog. Energy 2020, 45, 24518.
- [41] D. Dong, X. Shao, X. Hu, K. Chen, K. Xie, L. Yu, Z. Ye, P. Yang, G. Parkinson, C.-Z. Li, Int. J. Hydr. Energy 2016, 41, 19829.
- [42] S. M. Abd El Haleema, S. Abd El Wanees, Prot. Met. Phys. Chem. Surf. 2018. 54, 859.
- [43] P. Lettenmeier, S. Kolb, N. Sata, A. Fallisch, L. Zielke, S. Thiele, A. S. Gago, K. A. Friedrich, Energy Environ. Sci. 2017, 10, 2521.
- [44] B. Ghanbarian, A. G. Hunt, R. P. Ewing, M. Sahimi, Soil Sci. Soc. Am. J. 2013, 77, 1461.
- [45] M. C. Biesinger, B. P. Payne, A. P. Grosvenor, L. W. M. Lau, A. R. Gerson, R. S. C. Smart, Appl. Surf. Sci. 2011, 257, 2717.
- [46] J. F. Moulder, W. F. Stickle, P. E. Sobo, K. D. Bomben, Handbook of X-Ray photoelectron spectroscopy, 1st ed., Perkin-Elmer 421 Corporation, Eden Prairie, Minnesota, USA 55344, 1992,
- [47] M. El-Kemary, N. Nagy, I. El-Mehasseb, Mater. Sci. Semicond 2013, 16, 1747.
- [48] L. O. Alema 'n-Va 'zqueza, E. Torres-Garcı' aa, J. R. Villago 'mez-Ibarrab, J. L. Cano-Domi 'ngueza, *Catal. Lett.* **2005**, *100*, 219.
- [49] J. Li, P. Li, J. Li, Z. Tian, F. Yu, Catalysts 2019, 9, 506.
- [50] L. Barrientos, S. Rodriguez-Llamazares, J. Merchani, P. Jara, N. Yutronic, V. Lavayen, J. Chil. Chem. Soc. 2009, 54, 4.
- [51] S.-J. Hong, H.-J. Mun, B.-J. Kim, Y.-S. Kim, Micromachines 2021, 12, 1168.
- [52] K. Lota, A. Sierczynska, G. Lota, Int. J. Electrochem 2011, 1.
- [53] R. Hamidi, R. Khoshbin, R. Karimzadeh, *RSC Adv.* **2020**, *10*, 12439.
- [54] D. Wu, R. Shen, R. Yang, W. Ji, M. Jiang, W. Ding, L. Peng, Sci Rep 2017, 7, 44697.
- [55] G. S. Bajad, S. K. Tiwari, R. P. Vijayakumar, Materials Science and Engineering 2015, 194, 68.
- [56] L. O. Alema´n-Va´zqueza, E. Torres-Garcı´a, J. R. Villago´mez-Ibarra, J. L. Cano-Domı´nguez, *Catal. Lett.* **2005**, *100*, 3.

16146840, 0, Downloaded from https://onlinelibrary.wiley.com/doi/10.1002/ænm.202405285 by Dtsch Zentrum F. Luft-U. Raum Fahrt In D. Helmholtz Gemein

Wiley Online Library on [13/02/2025]. See the Terms

on Wiley Online Library for rules of use; OA articles are governed by the applicable Creative Commons

www.advancedsciencenews.com

- [57] E. G. Temam, H. B. Temam, S. Benramache, Chin. Phys. B 2015, 24, 108202.
- [58] H. Janssen, J. C. Bringmann, B. Emonts, V. Schroeder, Int. J. Hydrog. 2004, 29, 759.
- [59] L. Wang, T. Weissbach, R. Reissner, A. Ansar, A. S. Gago, S. Holdcroft, K. A. Friedrich, ACS Appl. Energy Mater 2019, 2, 7903.
- [60] C.-I. Lin, J.-H. Tsai, J.-Z. Chen, RSC Adv. 2020, 10, 11166.
- [61] E. German, R. Faccio, Á. W. Mombrú, Appl. Surf. Sci. 2017, 426, 1182.
- [62] R. Hesse, T. Chassé, R. Szargan, Fresenius' journal of analytical chemistry 1999, 365, 48.
- [63] J. J. Yeh, I. Lindau, Atomic data and nuclear data tables 1985, 32, 1.
- [64] P. Hohenberg, W. Kohn, Phys. Rev. 1964, 136, B864.
- [65] W. Kohn, L. J. Sham, Phys. Rev. 1965, 140, A1133.
- [66] G. Kresse, J. Furthmüller, Phys. Rev. B 1996, 54, 11169.

- [67] G. Kresse, J. Furthmüller, Comput. Mater. Sci. 1996, 6, 15.
- [68] G. Kresse, J. Hafner, Phys. Rev. B 1993, 47, 558.
- [69] G. Kresse, J. Hafner, Phys. Rev. B 1994, 49, 14251.
- [70] G. Kresse, D. Joubert, Phys. Rev. B 1999, 59, 1758.
- [71] P. E. Blöchl, Phys. Rev. B 1994, 50, 17953.
- [72] J. P. Perdew, K. Burke, M. Ernzerhof, Phys. Rev. Lett. 1996, 77, 3865.
- [73] J. P. Perdew, K. Burke, M. Ernzerhof, Phys. Rev. Lett. 1997, 78, 1396.
- [74] E. German, R. Faccio, A. W. Mombrú, Appl. Surf. Sci. 2018, 428, 118.
- [75] M. Esteves, L. Fernández-Werner, F. Pignanelli, B. Montenegro, M. Belluzzi, M. Pistón, M. R. Chialanza, R. Faccio, Á. W. Mombrú, Ceram. Int. 2019, 45, 708.
- [76] S. Grimme, J. Antony, S. Ehrlich, S. Krieg, J. Chem. Phys. 2010, 132, 154104.
- [77] S. Grimme, S. Ehrlich, L. Goerigk, J. Comput. Chem. 2011, 32, 1456.